

1

²A SEARCH FOR LONG-LIVED, CHARGED, SUPERSYMMETRIC PARTICLES
³USING IONIZATION WITH THE ATLAS DETECTOR

4

BRADLEY AXEN

5

September 2016 – Version 0.18

6



⁸ Bradley Axen: *A Search for Long-Lived, Charged, Supersymmetric Particles using Ion-
⁹ ization with the ATLAS Detector*, Subtitle, © September 2016

10

Usually a quotation.

11

Dedicated to.

₁₂ ABSTRACT

₁₃ How to write a good abstract:

₁₄ <https://plg.uwaterloo.ca/~migod/research/beck00PSLA.html>

₁₅ PUBLICATIONS

₁₆ Some ideas and figures have appeared previously in the following publications:

₁₇

₁₈ Put your publications from the thesis here. The packages `multibib` or `bibtopic`
₁₉ etc. can be used to handle multiple different bibliographies in your document.

²¹ ACKNOWLEDGEMENTS

²² Put your acknowledgements here.

²³

²⁴ And potentially a second round.

²⁵

26 CONTENTS

27	I	INTRODUCTION	1
28	1	INTRODUCTION	3
29	II	THEORETICAL CONTEXT	5
30	2	STANDARD MODEL	7
31	2.1	Particles	7
32	2.2	Interactions	8
33	2.3	Limitations	8
34	3	SUPERSYMMETRY	9
35	3.1	Motivation	9
36	3.2	Structure	9
37	3.3	Phenomenology	9
38	4	LONG-LIVED PARTICLES	11
39	4.1	Mechanisms	11
40	4.1.1	Examples in Supersymmetry	11
41	4.2	Phenomenology	11
42	4.2.1	Disimilarities to Prompt Decays	11
43	4.2.2	Characteristic Signatures	11
44	III	EXPERIMENTAL STRUCTURE AND RECONSTRUCTION	13
45	5	THE LARGE HADRON COLLIDER	15
46	5.1	Injection Chain	15
47	5.2	Design and Parameters	15
48	5.3	Luminosity	15
49	6	THE ATLAS DETECTOR	17
50	6.1	Coordinate System	17
51	6.2	Magnetic Field	17
52	6.3	Inner Detector	17
53	6.3.1	Pixel Detector	17
54	6.3.2	Semiconductor Tracker	17
55	6.3.3	Transition Radiation Tracker	17
56	6.4	Calorimetry	17
57	6.4.1	Electromagnetic Calorimeters	17
58	6.4.2	Hadronic Calorimeters	17
59	6.4.3	Forward Calorimeters	17
60	6.5	Muon Spectrometer	17
61	6.6	Trigger	17
62	6.6.1	Trigger Scheme	17
63	6.6.2	Missing Transverse Energy Triggers	17
64	7	EVENT RECONSTRUCTION	19
65	7.1	Tracks and Vertices	19

66	7.1.1	Track Reconstruction	19
67	7.1.2	Vertex Reconstruction	19
68	7.2	Jets	19
69	7.2.1	Topological Clustering	19
70	7.2.2	Jet Energy Scale	19
71	7.2.3	Jet Energy Scale Uncertainties	19
72	7.2.4	Jet Energy Resolution	19
73	7.3	Electrons	19
74	7.3.1	Electron Identification	19
75	7.4	Muons	19
76	7.4.1	Muon Identification	19
77	7.5	Missing Transverse Energy	19
78	IV	CALORIMETER RESPONSE	21
79	8	RESPONSE MEASUREMENT WITH SINGLE HADRONS	23
80	8.1	Overview and Motivation	23
81	8.2	Dataset and Simulation	24
82	8.2.1	Data Samples	24
83	8.2.2	Simulated Samples	24
84	8.2.3	Event Selection	24
85	8.3	Inclusive Hadron Response	25
86	8.3.1	E/p Distribution	25
87	8.3.2	Zero Fraction	27
88	8.3.3	Neutral Background Subtraction	27
89	8.3.4	Corrected Response	29
90	8.4	Identified Particle Response	32
91	8.4.1	Decay Reconstruction	33
92	8.4.2	Identified Response	33
93	8.4.3	Additional Species in Simulation	35
94	8.5	Summary	36
95	9	JET ENERGY RESPONSE AND UNCERTAINTY	39
96	9.1	Jet Energy Response in Simulation	39
97	9.2	Jet Energy Uncertainty	39
98	V	SEARCH FOR LONG-LIVED PARTICLES	41
99	10	LONG-LIVED PARTICLES IN ATLAS	43
100	10.1	Overview and Characteristics	43
101	10.2	Simulation	43
102	11	EVENT SELECTION	45
103	11.1	Trigger	45
104	11.2	Kinematics and Isolation	45
105	11.3	Standard Model Rejection	45
106	11.4	Ionization	45
107	11.4.1	dE/dx Calibration	45
108	11.4.2	Mass Estimation	45
109	12	BACKGROUND ESTIMATION	47

110	12.1	Background Sources	47
111	12.2	Prediction Method	47
112	12.3	Validation and Uncertainty	47
113	13	SYSTEMATIC UNCERTAINTIES AND RESULTS	49
114	13.1	Systematic Uncertainties	49
115	13.2	Final Yields	49
116	14	INTERPRETATION	51
117	14.1	Cross Sectional Limits	51
118	14.2	Mass Limits	51
119	14.3	Context for Long-Lived Searches	51
120	VI	CONCLUSIONS	53
121	15	SUMMARY AND OUTLOOK	55
122	15.1	Summary	55
123	15.2	Outlook	55
124	VII	APPENDIX	57
125	A	INELASTIC CROSS SECTION	59
126	B	APPENDIX TEST	61
127	B.1	Appendix Section Test	61
128	B.1.1	Appendix Subection Test	61
129	B.2	A Table and Listing	61
130	B.3	Some Formulas	62
131		BIBLIOGRAPHY	65

132 LIST OF FIGURES

133	Figure 1	The particle content of the Standard Model.	8
134	Figure 2	An illustration (a) of the E/p variable used throughout this paper. The red energy deposits come from the charged particle targeted for measurement, while the blue energy deposits are from nearby neutral particles and must be subtracted. The same diagram (b) for the neutral-background selection, described in Section 8.3.3.	26
135			
136			
137			
138			
139			
140	Figure 3	The E/p distribution and ratio of simulation to data for isolated tracks with (a) $ \eta < 0.6$ and $1.2 < p/\text{GeV} < 1.8$ and (b) $ \eta < 0.6$ and $2.2 < p/\text{GeV} < 2.8$	26
141			
142			
143	Figure 4	The fraction of tracks as a function (a, b) of momentum, (c, d) of interaction lengths with $E \leq 0$ for tracks with positive (on the left) and negative (on the right) charge.	28
144			
145			
146			
147	Figure 5	$\langle E/p \rangle_{\text{BG}}$ as a function of the track momentum and (a) $ \eta < 0.6$, (b) $0.6 < \eta < 1.1$, and as a function of the track pseudorapidity and (c) $1.2 < p/\text{GeV} < 1.8$, (d) $1.8 < p/\text{GeV} < 2.2$	29
148			
149			
150			
151	Figure 6	$\langle E/p \rangle_{\text{COR}}$ as a function of track momentum, for tracks with (a) $ \eta < 0.6$, (b) $0.6 < \eta < 1.1$, (c) $1.8 < \eta < 1.9$, and (d) $1.9 < \eta < 2.3$	30
152			
153			
154	Figure 7	$\langle E/p \rangle_{\text{COR}}$ calculated using LCW-calibrated topological clusters as a function of track momentum for tracks with (a) zero or more associated topological clusters or (b) one or more associated topological clusters.	31
155			
156			
157			
158	Figure 8	Comparison of the $\langle E/p \rangle_{\text{COR}}$ for tracks with (a) less than and (b) greater than 20 hits in the TRT.	32
159			
160	Figure 9	Comparison of the $\langle E/p \rangle_{\text{COR}}$ for (a) positive and (b) negative tracks as a function of track momentum for tracks with $ \eta < 0.6$	32
161			
162			
163	Figure 10	Comparison of the E/p distributions for (a) positive and (b) negative tracks with $0.8 < p/\text{GeV} < 1.2$ and $ \eta < 0.6$, in simulation with the FTFP_BERT and QGSP_BERT physics lists.	33
164			
165			
166			
167	Figure 11	The reconstructed mass peaks of (a) K_S^0 , (b) Λ , and (c) $\bar{\Lambda}$ candidates.	34
168			
169	Figure 12	The E/p distribution for isolated (a) π^+ , (b) π^- , (c) proton, and (d) anti-proton tracks.	35
170			
171	Figure 13	The fraction of tracks with $E \leq 0$ for identified (a) π^+ and π^- , and (b) proton and anti-proton tracks	36
172			

173	Figure 14	The difference in $\langle E/p \rangle$ between (a) π^+ and π^- (b) p and π^+ , and (c) \bar{p} and π^-	37
174		$\langle E/p \rangle_{\text{COR}}$ as a function of track momentum for (a) π^+ tracks and (b) π^- tracks.	37
175	Figure 15		
176			
177	Figure 16	The ratio of the calorimeter response to single particles of various species to the calorimeter response to π^+ with the physics list FTFP_BERT.	37
178			
179			

180 LIST OF TABLES

181	Table 1	Autem usu id	61
-----	---------	------------------------	----

¹⁸² LISTINGS

¹⁸³ Listing 1	A floating example (<code>listings</code> manual)	62
--------------------------	--	----

¹⁸⁴ ACRONYMS

¹⁸⁵ EG Example

186

PART I

187

INTRODUCTION

188

You can put some informational part preamble text here.

1

189

190 INTRODUCTION

191

PART II

192

THEORETICAL CONTEXT

193

You can put some informational part preamble text here.

2

194

195 STANDARD MODEL

196 The Standard Model of particle physics seeks to explain the symmetries and in-
197 teractions of all currently discovered fundamental particles. It has been tested by
198 several generations of experiments and has been remarkably successful, no sig-
199 nificant deviations have been found. The Standard Model provides predictions
200 in particle physics for interactions up to the Planck scale (10^{15} - 10^{19} GeV).

201 The theory itself is a quantum field theory grown from an underlying $SU(3) \times$
202 $SU(2) \times U(1)$ that requires the particle content and quantum numbers consist-
203 ent with experimental observations (see Section 2.1). Each postulated symme-
204 try is accompanied by an interaction between particles through gauge invari-
205 ance. These interactions are referred to as the Strong, Weak, and Electromag-
206 netic forces, which are discussed in Section 2.2.

207 Although this model has been very predictive, the theory is incomplete; for
208 example, it is not able to describe gravity or astronomically observed dark matter.
209 These limitations are discussed in more detail in Section 2.3.

210 21 PARTICLES

211 The most familiar matter in the universe is made up of protons, neutrons, and
212 electrons. Protons and neutrons are composite particles, however, and are made
213 up in turn by particles called quarks. Quarks carry both electric charge and color
214 charge, and are bound in color-neutral combinations called baryons. The elec-
215 tron is an example of a lepton, and carries only electric charge. Another type
216 of particle, the neutrino, does not form atomic structures in the same way that
217 quarks and leptons do because it carries no color or electric charge. Collectively,
218 these types of particles are known as fermions, the group of particles with half-
219 integer spin.

220 There are three generations of fermions, although familiar matter is formed
221 predominantly by the first generation. The generations are identical except for
222 their masses, which increase in each generation by convention. In addition, each
223 of these particles is accompanied by an antiparticle, with opposite-sign quantum
224 numbers but the same mass.

225 The fermions comprise what is typically considered matter, but there are
226 additional particles that are mediators of interactions between those fermions.
227 These mediators are known as the gauge bosons, gauge in that their existence
228 is required by gauge invariance (discussed further in Section 2.2) and bosons in
229 that they have integer spin. The boson which mediates the electromagnetic force
230 is the photon, the first boson to be discovered; it has no electric charge, no mass,
231 and a spin of 1. There are three spin-1 mediators of the weak force, the two W
232 bosons and the Z boson. The W bosons have electric charge of ± 1 and a mass of
233 80.385 ± 0.015 GeV, while the Z boson is neutral and has a mass of $91.1876 \pm$

234 0.0021 GeV. The strong force is mediated by eight particles called gluons, which
 235 are massless and electrically neutral but do carry color charge.

236 The final particle present in the Standard Model is the Higgs boson, which was
 237 recently observed for the first time by experiments at CERN in 2012. It is electric-
 238 ically neutral, has a mass of 125.7 ± 0.4 GeV, and is the only spin-0 particle yet to
 239 be observed. The Higgs boson is the gauge boson associated with the mechanism
 240 that gives a mass to the W and Z bosons.

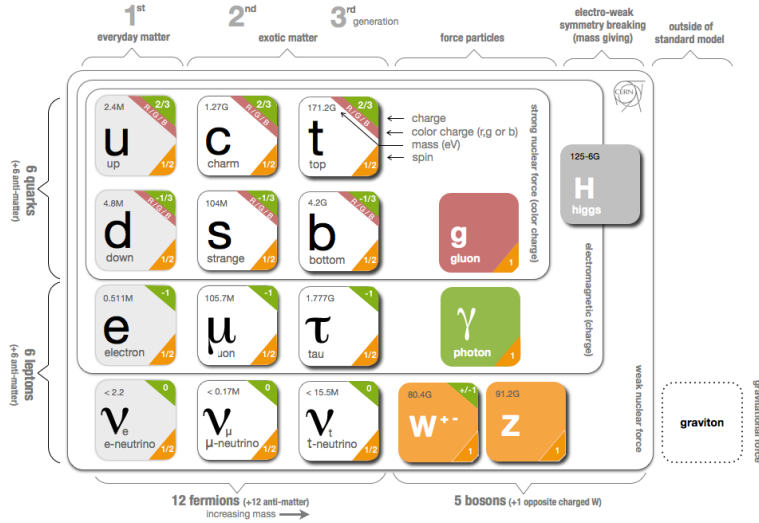


Figure 1: The particle content of the Standard Model.

241 Together these particles form the entire content of the Standard Model, and
 242 are summarized in Figure 1. These are the particles that constitute the observable
 243 universe and all the so-far-observed interactions within it.

244 2.2 INTERACTIONS

245 The interactions predicted and described by the Standard Model are fundamen-
 246 tally tied to the particles within it, both in that they describe the way those par-
 247 ticles can influence each other and also in that the existence of the interactions
 248 requires the existence of some particles (the gauge bosons).

249 2.3 LIMITATIONS

3

250

251 SUPERSYMMETRY

252 3.1 MOTIVATION

253 3.2 STRUCTURE

254 3.3 PHENOMENOLOGY

4

255

256 LONG-LIVED PARTICLES

257 4.1 MECHANISMS

258 4.1.1 EXAMPLES IN SUPERSYMMETRY

259 4.2 PHENOMENOLOGY

260 4.2.1 DISIMILARITIES TO PROMPT DECAYS

261 4.2.2 CHARACTERISTIC SIGNATURES

262

PART III

263

EXPERIMENTAL STRUCTURE AND RECONSTRUCTION

264

You can put some informational part preamble text here.

5

265

266 THE LARGE HADRON COLLIDER

267 5.1 INJECTION CHAIN

268 5.2 DESIGN AND PARAMETERS

269 5.3 LUMINOSITY

6

270

271 THE ATLAS DETECTOR

272 6.1 COORDINATE SYSTEM

273 6.2 MAGNETIC FIELD

274 6.3 INNER DETECTOR

275 6.3.1 PIXEL DETECTOR

276 6.3.2 SEMICONDUCTOR TRACKER

277 6.3.3 TRANSITION RADIATION TRACKER

278 6.4 CALORIMETRY

279 6.4.1 ELECTROMAGNETIC CALORIMETERS

280 6.4.2 HADRONIC CALORIMETERS

281 6.4.3 FORWARD CALORIMETERS

282 6.5 MUON SPECTROMETER

283 6.6 TRIGGER

284 6.6.1 TRIGGER SCHEME

285 6.6.2 MISSING TRANSVERSE ENERGY TRIGGERS

7

286

287 EVENT RECONSTRUCTION

288 The ATLAS experiment combines measurements in the subdetectors to form a
289 cohesive picture of each physics event.

290 7.1 TRACKS AND VERTICES

291 7.1.1 TRACK RECONSTRUCTION

292 7.1.1.1 NEURAL NETWORK

293 7.1.1.2 PIXEL DE/DX

294 7.1.2 VERTEX RECONSTRUCTION

295 7.2 JETS

296 7.2.1 TOPOLOGICAL CLUSTERING

297 7.2.2 JET ENERGY SCALE

298 7.2.3 JET ENERGY SCALE UNCERTAINTIES

299 7.2.4 JET ENERGY RESOLUTION

300 7.3 ELECTRONS

301 7.3.1 ELECTRON IDENTIFICATION

302 7.4 MUONS

303 7.4.1 MUON IDENTIFICATION

304 7.5 MISSING TRANSVERSE ENERGY

305

PART IV

306

CALORIMETER RESPONSE

307

You can put some informational part preamble text here.

310 8.1 OVERVIEW AND MOTIVATION

311 As discussed in Section 7.2, colored particles produced in collisions hadronize
312 into jets of multiple individual hadrons. As jets form a major component of many
313 physics analyses at ATLAS, it is crucial to carefully calibrate the measurement of
314 jet energies and to derive an uncertainty on that measurement. These uncertain-
315 ties have often been the dominant systematic uncertainty in high-energy analy-
316 ses at the LHC.

317 One approach to understanding jet physics in the ATLAS calorimetry is to
318 evaluate the calorimeter response to individual hadrons; measurements of indi-
319 vidual hadrons can be used to build up an understanding of the jets that they form.
320 The redundancy of the momentum provided by the tracking system and the en-
321 ergy provided by the calorimeter provides an opportunity to study calorimeter
322 response using real collisions, as described further in Section 8.3.

323 A number of interesting factors compromise calorimeter response, and ex-
324 tracting these separately provides insight into many aspects of jet modeling. First,
325 many charged hadrons interact with the material of the detector prior to reach-
326 ing the calorimeters and thus do not deposit any energy. Comparing this effect in
327 data and simulation is a powerful tool in validating the interactions of particles
328 with the material of the detector as well as the model of the detector geometry
329 in simulation, see Section 8.3.2. The particles which do reach the calorimeter de-
330 posit their energy into individual cells, which are then clustered to measure full
331 energy deposits. Comparing the response in data to simulated hadrons provides
332 a direct evaluation of several aspects of simulation: noise in the calorimeters, the
333 showering of hadronic particles, and the energy deposited by particles in mat-
334 ter, among others (Section 8.3.4). These measurements are extended to explore
335 several additional effects, such as the dependence on charge or the individual
336 calorimeter layer in Section 8.3.4.1.

337 The above studies all use an inclusive selection of charged particles, which are
338 compromised predominantly of pions, kaons, and (anti)protons. It is also inter-
339 esting to measure the particle types separately to evaluate the simulated inter-
340 actions of each particle, particularly at low energies where differences between
341 species are very relevant. Pions and (anti)protons can be identified through de-
342 cays of long-lived particles, in particular Λ , $\bar{\Lambda}$, and K_S^0 , and then used to measure
343 response as described above. This is discussed in detail in Section 8.4.

344 Together, these measurements in data provide a thorough understanding of
345 the way hadrons interact with the ATLAS detector and can be used to build up a
346 description of jets, as seen in Chapter 9. The results in this chapter use data col-
347 lected at 7 and 8 TeV collected in 2010 and 2012, respectively. Both are included
348 as the calorimeter was repaired and recalibrated between those two data-taking

349 periods. Both sets of data are compared to an updated simulation that includes
 350 new physics models provided by Geant4 [9] and improvements in the detector
 351 description [2, 5]. These results are published in EPJC [6] and can be compared to
 352 a similar measurement performed in 2009 and 2010 [4], which used the previous
 353 version of the simulation framework [1].

354 8.2 DATASET AND SIMULATION

355 8.2.1 DATA SAMPLES

356 The two datasets used in this chapter are taken from dedicated low-pileup runs
 357 where the fraction of events with multiple interactions was negligible, to facili-
 358 tate measurement of isolated hadrons. The 2012 dataset at $\sqrt{s} = 8$ TeV contains 8
 359 million events and corresponds to an integrated luminosity of 0.1 nb^{-1} . The 2010
 360 dataset at $\sqrt{s} = 7$ TeV contains 3 million events and corresponds to an integrated
 361 luminosity of 3.2 nb^{-1} . This last dataset was also used in the 2010 results [4], but
 362 have since been reanalyzed with an updated detector description of the material
 363 and alignment.

364 8.2.2 SIMULATED SAMPLES

365 The two datasets above are compared to simulated single-, double-, and non-
 366 diffractive events generated with Pythia8 [28] using the A2 configuration of
 367 hadronization [3] and the MSTW 2008 parton-distribution function set [24, 27].
 368 The conditions and energies for each run are matched in the two simulations.

369 To evaluate the interaction of hadrons with detector material, the simulation
 370 uses two different collections of hadronic physics models, called physics lists, in
 371 Geant4 9.4 [26]. The first, QGSP_BERT, combines the Bertini intra-nuclear
 372 cascade [14, 21, 23] below 9.9 GeV, a parametrized proton inelastic model from
 373 9.5 to 25 GeV [18], and a quark-gluon string model above 12 GeV [10, 11, 15, 16,
 374 19]. The second, FTFP_BERT, combines the Bertini intra-nuclear cascade [14, 21,
 375 23] below 5 GeV and the Fritiof model [12, 13, 20, 25] above 4 GeV. In either list,
 376 where multiple models overlap, the transition between the two models is ensured
 377 to be smooth.

378 8.2.3 EVENT SELECTION

379 The event selection for this study is minimal, as the only requirement is selecting
 380 good-quality events with an isolated track. Such events are triggered by requir-
 381 ing at least two hits in the minimum-bias trigger scintillators. After trigger, each
 382 event is required to have exactly one reconstructed vertex, and that vertex is re-
 383 quired to have four or more associated tracks.

384 The particles which enter into the response measurements are first identified
 385 as tracks in the inner detector. To ensure a reliable momentum measurement,
 386 these tracks are required to have at least one hit in the pixel detector, six hits in

387 the SCT, and small longitudinal and transverse impact parameters with respect
 388 to the primary vertex [4]. For the majority of the measurements in this chapter,
 389 the track is additionally required to have 20 hits in the TRT, which significantly
 390 reduces the contribution from tracks which undergo nuclear interactions.
 391 This requirement and its effect is discussed in more detail in Section 8.3.4.1. In
 392 addition, tracks are rejected if there is another track which extrapolates to the
 393 calorimeter within a cone of $\Delta R = \sqrt{(\Delta\phi)^2 + (\Delta\eta)^2} < 0.4$. This requirement
 394 guarantees that the contamination of energy from nearby charged particles is
 395 negligible [4].

396 8.3 INCLUSIVE HADRON RESPONSE

397 The calorimeter response is more precisely defined as the ratio of the measured
 398 calorimeter energy to the true energy carried by the particle, although this true
 399 energy is unknown. For charged particles, however, the inner detector provides
 400 a very precise measurement of momentum (with uncertainty less than 1%) that
 401 can be used as a proxy for true energy. The ratio of the energy deposited by the
 402 charged particle in the calorimeter, E , to its momentum measured in the inner
 403 detector p , forms the calorimeter response measure called E/p . Though the dis-
 404 tribution of E/p is interesting, two aggregated quantities are more directly use-
 405 ful: $\langle E/p \rangle$, the average of E/p within a given subset of particles, and the zero
 406 fraction, the fraction of particles with no associated clusters in the calorimeter.

407 The calorimeter energy assigned to a track particle is defined using either
 408 clusters. The clusters are formed using a 4–2–0 algorithm [7] that begins with
 409 seeds requiring at least 4 times the calorimeter average noise. The neighboring
 410 cells with at least twice that noise threshold are then added to the cluster, and all
 411 bounding cells are then added with no requirement. This algorithm minimizes
 412 noise contributions through its seeding process, and including the additional lay-
 413 ers improves the energy resolution [29]. The clusters are associated to a given
 414 track if they fall within a cone of $\Delta R = 0.2$ of the extrapolated position of the
 415 track, which includes about 90% of the energy on average [4]. This construction
 416 is illustrated in Figure 2.

417 8.3.1 E/P DISTRIBUTION

418 The E/p distributions measured in both data and simulation are shown in Fig-
 419 ure 3 for two example bins of track momentum and for tracks in the central
 420 region of the detector. These distribution show several important features of
 421 the E/p observable. The large content in the bin at $E = 0$ comes from tracks that
 422 have no associated cluster, as mentioned previously these are due to interactions
 423 with detector material prior to reaching the calorimeter or the energy deposit be-
 424 ing insufficiently large to generate a seed, and are discussed in Section 8.3.2. The
 425 small negative tail comes from similar tracks that do not deposit any energy in
 426 the calorimeter but are randomly associated to a noise cluster. The long positive
 427 tail above 1.0 comes from the contribution of neutral particles. Nearby neutral
 428 particles deposit (sometimes large) additional energy in the calorimeter but do

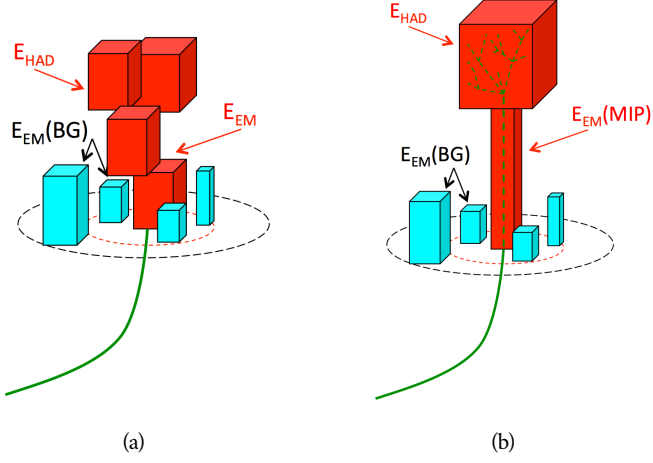


Figure 2: An illustration (a) of the E/p variable used throughout this paper. The red energy deposits come from the charged particle targeted for measurement, while the blue energy deposits are from nearby neutral particles and must be subtracted. The same diagram (b) for the neutral-background selection, described in Section 8.3.3.

not produce tracks in the inner detector and so they cannot be rejected for isolation. Additionally the peak and mean of the distribution falls below 1.0 because of the loss of energy not found within the cone as well as the non-compensation of the calorimeter.

The data and simulation share the same features, but the high and low tails are significantly different. The simulated events tend to overestimate the contribution of neutral particle to the long tail, although this effect can be isolated as discussed in Section 8.3.3. Additionally, the simulated clusters have less noise on average, although this is a small effect on the overall response.

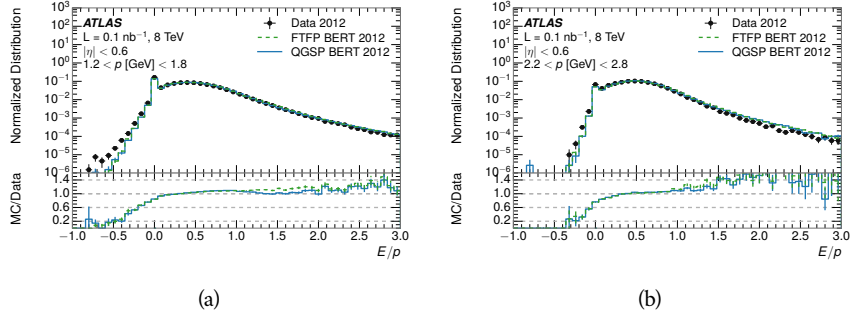


Figure 3: The E/p distribution and ratio of simulation to data for isolated tracks with (a) $|\eta| < 0.6$ and $1.2 < p/\text{GeV} < 1.8$ and (b) $|\eta| < 0.6$ and $2.2 < p/\text{GeV} < 2.8$.

438 8.3.2 ZERO FRACTION

439 The fraction of particles with no associated clusters, or similarly those with $E \leq$
 440 0, reflects the modeling of both the detector geometry and hadronic interactions.
 441 The zero fraction is expected to rise as the amount of material a particle traverses
 442 increases, while it is expected to decrease as the particle energy increases. This
 443 dependence can be seen in Figure 4, where the zero fraction in data and simula-
 444 tion is shown as a function of momentum and the amount of material measured
 445 in interaction lengths. The trends are similar between the 2010 and 2012 mea-
 446 surements. The zero fraction decreases with energy as expected. The amount of
 447 material in the detector increases with η , which provides a distribution of in-
 448 teraction lengths. As the data and simulation have significant disagreement in
 449 the zero fraction over a number of interaction lengths, the difference must be
 450 primarily from the modeling of hadronic interactions with detector material..

451 There is also a noticeable difference between positive at negative tracks at low
 452 momentum, which reflects the difference in response between protons and an-
 453 tiprotons. Antiprotons have significant model differences in the two physics lists,
 454 QGSP_BERT and FTFP_BERT, and this is evident in the lowest momentum bin
 455 of the data to simulation ratio. This difference is explored further in Section 8.4.

456 8.3.3 NEUTRAL BACKGROUND SUBTRACTION

457 The isolation requirement on hadrons is only effective in remove energy contri-
 458 bution from nearby charged particles. Nearby neutral particles, predominantly
 459 photons from π^0 decays, also add their energy to the calorimeter clusters, but
 460 mostly in the electromagnetic calorimeter. It is possible to measure this contri-
 461 bution, on average, using late-showering hadrons that minimally ionize in the
 462 electromagnetic calorimeter. Such particles are selected by requiring that they
 463 deposit less than 1.1 GeV in the EM calorimeter within a cone of $\Delta R < 0.1$
 464 around the track. To ensure that these particles are well measured, they are addi-
 465 tionally required to deposit between 40% and 90% of their energy in the hadronic
 466 calorimeter within the same cone.

467 These particle provide a clean sample to measure the nearby neutral back-
 468 ground because they do not deposit energy in the area immediately surrounding
 469 them in the EM calorimeter, as shown in Figure 2. So, the energy deposits in the
 470 region $0.1 < \Delta R < 0.2$ can be attributed to neutral particles alone. To estimate
 471 the contribution to the whole cone considered for the response measurement,
 472 that energy is scaled by a geometric factor of 4/3. This quantity, $\langle E/p \rangle_{\text{BG}}$, mea-
 473 sured in aggregate over a number of particles, gives the contribution to $\langle E/p \rangle$
 474 from neutral particles in the EM calorimeter. Similar techniques were used in
 475 the individual layers of the hadronic calorimeters to show that the background
 476 from neutrals is negligible in those layers [4].

477 The distribution of this background estimate is shown in Figure 5. Although
 478 the simulation captures the overall trend, it significantly overestimates the neu-
 479 tral contribution for tracks with momentum between 2 and 8 GeV. This effect
 480 was also seen in the tails of the E/p distributions in Figure 3. This difference is

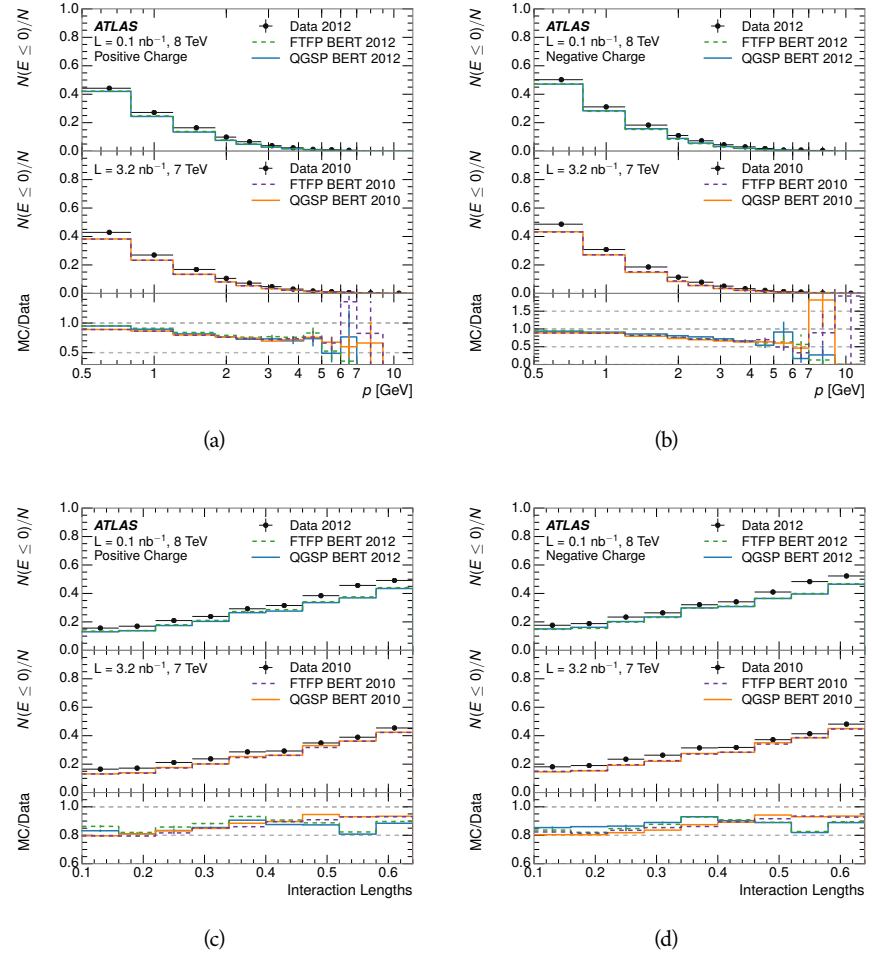


Figure 4: The fraction of tracks as a function (a, b) of momentum, (c, d) of interaction lengths with $E \leq 0$ for tracks with positive (on the left) and negative (on the right) charge.

likely due to the modeling of coherent neutral particle radiation in Pythia8, as the discrepancy does not depend on η and thus is unlikely to be a mismodeling of the detector. This difference can be subtracted to form a corrected average E/p , as in Section 8.3.4.

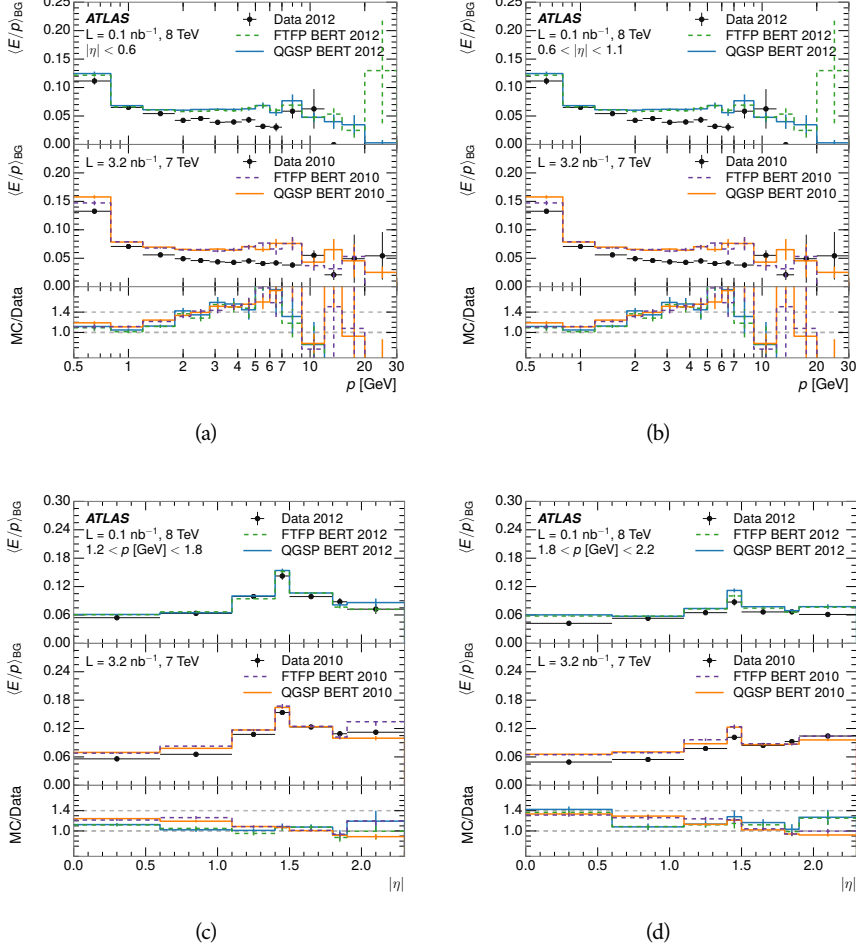


Figure 5: $\langle E/p \rangle_{BG}$ as a function of the track momentum and (a) $|\eta| < 0.6$, (b) $0.6 < |\eta| < 1.1$, and as a function of the track pseudorapidity and (c) $1.2 < p/\text{GeV} < 1.8$, (d) $1.8 < p/\text{GeV} < 2.2$.

8.3.4 CORRECTED RESPONSE

Figure 6 shows $\langle E/p \rangle_{COR}$ as a function of momentum for several bins of pseudorapidity. This corrected $\langle E/p \rangle_{COR} \equiv \langle E/p \rangle - \langle E/p \rangle_{BG}$ measures the average calorimeter response without the contamination of neutral particles. It is the most direct measurement of calorimeter response in that it is the energy measured for fully isolated hadrons. The correction is performed separately in data and simulation, so that the mismodeling of the neutral background in simulation is removed from the comparison of response. The simulation overestimates the

493 response at low momentum by about 5%, an effect that can be mostly attributed
 494 to the underestimation of the zero fraction mentioned previously.

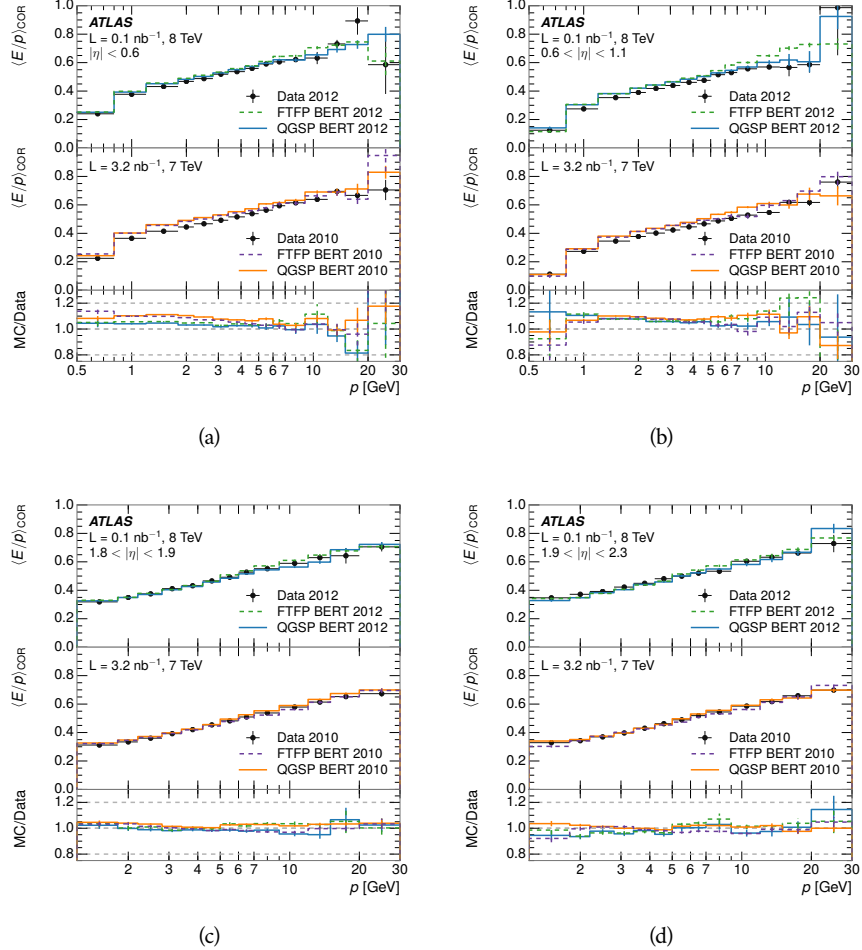


Figure 6: $\langle E/p \rangle_{\text{COR}}$ as a function of track momentum, for tracks with (a) $|\eta| < 0.6$, (b) $0.6 < |\eta| < 1.1$, (c) $1.8 < |\eta| < 1.9$, and (d) $1.9 < |\eta| < 2.3$.

495 The response measurement above used topological clustering at the EM scale,
 496 that is clusters were formed to measure energy but no corrections were applied
 497 to correct for expected effects like energy lost outside of the cluster or in unin-
 498 strumented material. It is also interesting to measure $\langle E/p \rangle_{\text{COR}}$ using local clus-
 499 ter weighted (LCW) energies, which accounts for those effects by calibrating the
 500 energy based on the properties of the cluster such as energy density and depth
 501 in the calorimeter. Figure ?? shows these distributions for tracks with zero or
 502 more clusters and separately for tracks with one or more clusters. The cali-
 503 bration moves $\langle E/p \rangle_{\text{COR}}$ significantly closer to 1.0, which is the purpose of the cali-
 504 bration. The agreement between data and simulation improves noticeably when
 505 at least one cluster is required, as this removes the contribution from the mis-
 506 modeling of zero fraction.

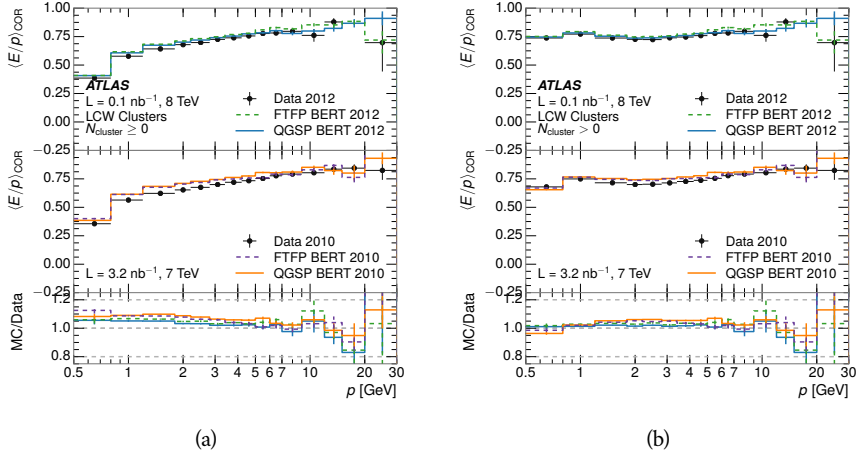


Figure 7: $\langle E/p \rangle_{\text{COR}}$ calculated using LCW-calibrated topological clusters as a function of track momentum for tracks with (a) zero or more associated topological clusters or (b) one or more associated topological clusters.

507 8.3.4.1 ADDITIONAL STUDIES

508 As has been seen in several previous measurements, the simulation does not
 509 correctly model the chance of a low momentum hadron to reach the calorimeter.
 510 Because of the consistent discrepancy across pseudorapidity and interaction
 511 lengths, this seems to be best explained by incomplete understanding of hadronic
 512 interactions with the detector. For example, a hadron that scatters off of a nu-
 513 cleus in the inner detector can be deflected through a significant angle and not
 514 reach the expected location in the calorimeter. In addition, these interaction can
 515 produce secondary particles that are difficult to model.

516 The requirement on the number of hits in the TRT reduces these effects by
 517 preferentially selecting tracks that do not undergo nuclear interactions. It is in-
 518 teresting to check how well the simulation models tracks with low numbers of
 519 TRT hits, where the nuclear interactions are much more likely. Figure ?? com-
 520 pares the distributions with $N_{\text{TRT}} < 20$ to $N_{\text{TRT}} > 20$ for real and simulated
 521 particles. As expected, the tracks with fewer hits are poorly modeled in the sim-
 522 ulation as $\langle E/p \rangle_{\text{COR}}$ differs by as much as 25% at low momentum.

523 Another interesting aspect of the simulation is the description of antiprotons
 524 at low momentum, where QGSP_BERT and FTFP_BERT have significant differ-
 525 ences. This can be seen to have an effect in the inclusive response measurement
 526 when separated into positive and negative charge. The $\langle E/p \rangle_{\text{COR}}$ distributions
 527 for positive and negative particles are shown in Figure 9, where a small differ-
 528 ence between QGSP_BERT and FTFP_BERT can be seen in the distribution for
 529 negative tracks. This is demonstrated more clearly in Figure 10, which shows
 530 the E/p distribution in the two simulations separated by charge. There is a clear
 531 difference around $E/p > 1.0$, which can be explained by the additional energy de-
 532 posited by the annihilation of the antiproton in the calorimeter that is modelled
 533 only in FTFP_BERT. This is also explored with data using identified antiprotons
 534 in Section 8.4.

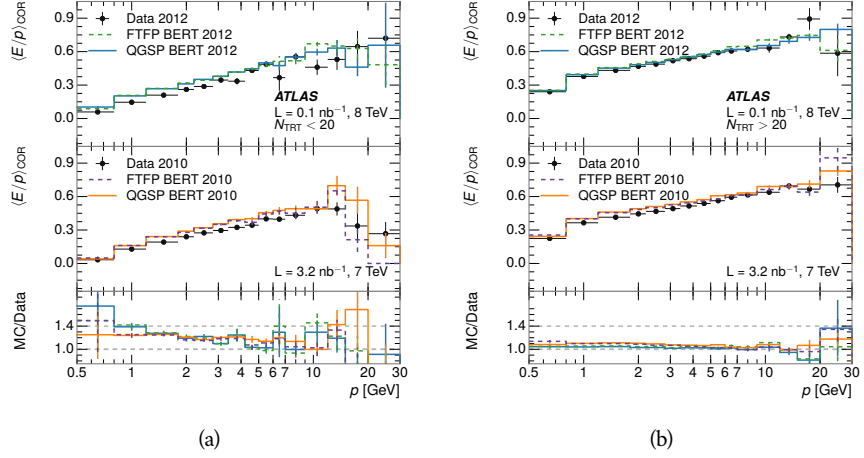


Figure 8: Comparison of the $\langle E/p \rangle_{\text{COR}}$ for tracks with (a) less than and (b) greater than 20 hits in the TRT.

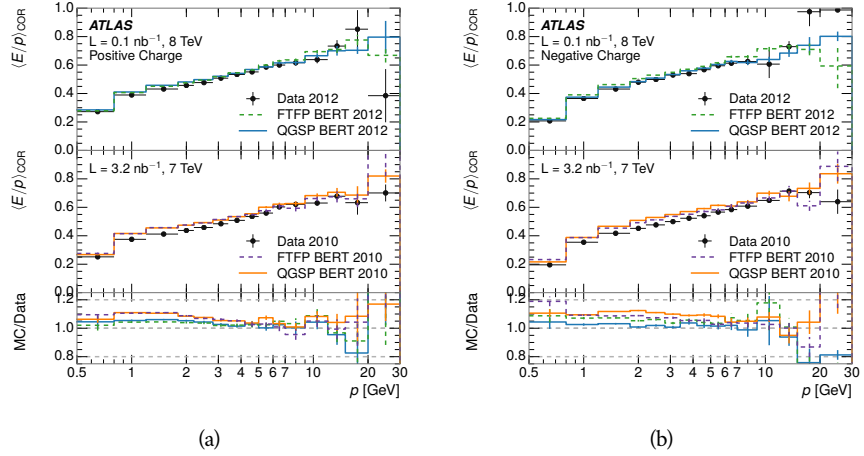


Figure 9: Comparison of the $\langle E/p \rangle_{\text{COR}}$ for (a) positive and (b) negative tracks as a function of track momentum for tracks with $|\eta| < 0.6$.

535 **NOTE: There are more studies that I skipped for brevity that could be
536 included if interesting. E/p in each calorimeter separately, E/p at different
537 cluster threshold settings, E/p with pileup. I also left out a lot of eta bins
538 that appear in the paper so that this section didn't turn into 20 pages of
539 plots.**

540 8.4 IDENTIFIED PARTICLE RESPONSE

541 The inclusive response measurement for hadrons can be augmented by measur-
542 ing the response for specific particle species. The simulation models each parti-
543 cle type separately, and understanding the properties of each is important in con-
544 straining the uncertainty on jets. In order to select and measure specific hadrons,

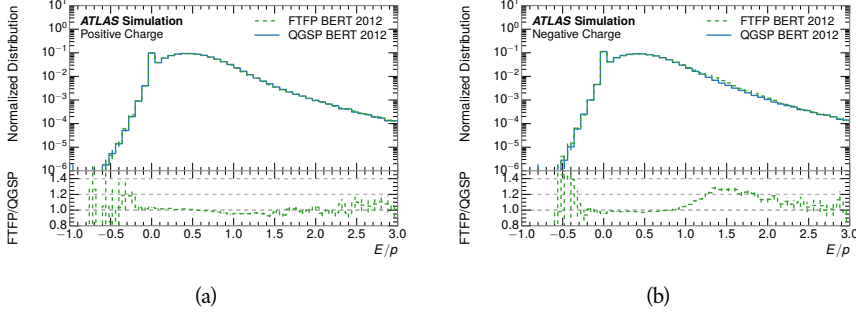


Figure 10: Comparison of the E/p distributions for (a) positive and (b) negative tracks with $0.8 < p/\text{GeV} < 1.2$ and $|\eta| < 0.6$, in simulation with the FTFP_BERT and QGSP_BERT physics lists.

545 this section relies on the displaced decays of long-lived particles. Such decays can
 546 be identified by reconstructing secondary vertices, and the particles used decay
 547 predominantly to specific hadrons. In particular, Λ , $\bar{\Lambda}$, and K_S^0 can be used to
 548 select a pure sample of protons, antiprotons, and pions, respectively.

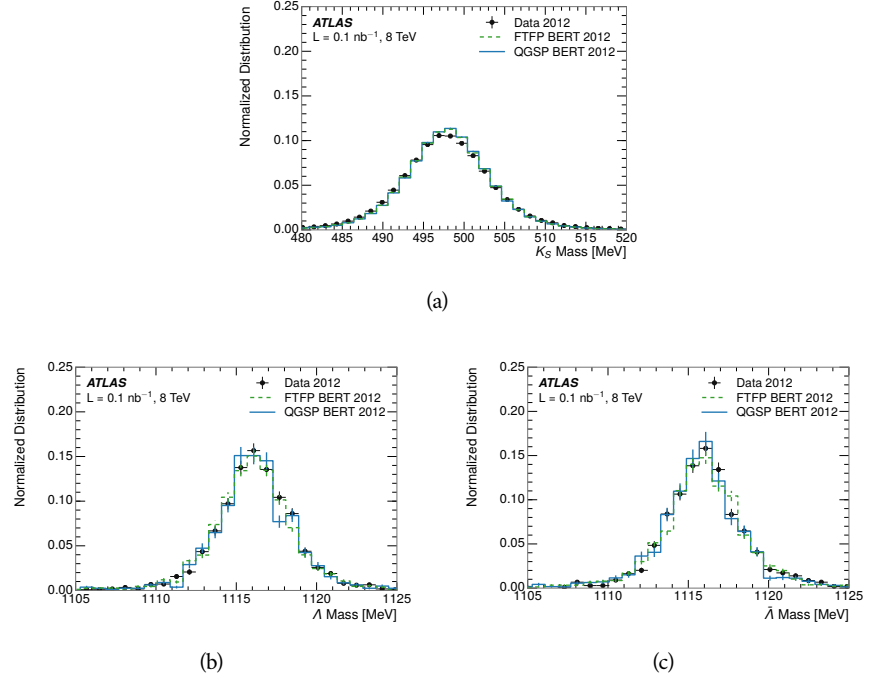
549 8.4.1 DECAY RECONSTRUCTION

550 The measurement of response for identified particles uses the same selection
 551 as for inclusive particles (Section 8.2.3, with a few additions. Each event used
 552 is required to have at least one secondary vertex, and the tracks are required
 553 to match to that vertex rather than the primary vertex. Pions are selected from
 554 decays of $K_S^0 \rightarrow \pi^+ \pi^-$, which is the dominant decay for K_S^0 to charged particles.
 555 Protons are selected from decays of $\Lambda \rightarrow \pi^- p$ and antiprotons from $\bar{\Lambda} \rightarrow \pi^+ \bar{p}$,
 556 which are similarly the dominant decays of Λ and $\bar{\Lambda}$ to charged particles. The
 557 species of parent hadron in these decays is determined by reconstructing the
 558 mass of the tracks associated to the secondary vertex. The sign of the higher
 559 momentum decay particles can distinguish between Λ and $\bar{\Lambda}$, which of course
 560 have the same mass, as the proton or antiproton is kinematically favored to have
 561 higher momentum. Examples of the reconstructed masses used to select these
 562 decays are shown in Figure 11.

563 There are a number of sources of backgrounds for these identified particles,
 564 including nuclear interactions and combinatoric sources. These are suppressed
 565 by the kinematic requirements on the tracks as well as an additional veto which
 566 removes candidates that are consistent with both a Λ or $\bar{\Lambda}$ and a K_S^0 hypothesis,
 567 which is possible because of the different assumptions on particle mass in each
 568 case [4]. After these requirements, the backgrounds are found to be negligible
 569 compared to the statistical errors on these measurements.

570 8.4.2 IDENTIFIED RESPONSE

571 With these techniques the E/p distributions are extracted in data and simulation
 572 for each particle species and shown in Figure 12. These distributions are shown

Figure 11: The reconstructed mass peaks of (a) K_S^0 , (b) Λ , and (c) $\bar{\Lambda}$ candidates.

for a particular bin of E_a ($2.2 < E_a/\text{GeV} < 2.8$), rather than p . E_a is the energy available to be deposited in the calorimeter: for pions $E_a = \sqrt{p^2 + m^2}$, for protons $E_a = \sqrt{p^2 + m^2} - m$, and for antiprotons $E_a = \sqrt{p^2 + m^2} + m$. The features of the E/p distributions are similar to the inclusive case. There is a small negative tail from noise and a large fraction of tracks with zero energy from tracks which do not reach the calorimeter. The long positive tail is noticeably more pronounced for antiprotons because of the additional energy generated by the annihilation in addition to the neutral background.

The zero fraction is further explored in Figure 13 for pions and protons in data and simulation. The simulation consistently underestimates the zero fraction independent of particle species, which implies that this discrepancy is not caused by the model of a particular species but rather a feature common to all.

It is also interesting to compare the response between the different particle species. One approach to do this is to measure the difference in $\langle E/p \rangle$ between two types, which has the advantage of removing the neutral background. These differences are shown in various combinations in Figure 14. The response for π^+ is greater on average than the response to π^- because of a charge-exchange effect which causes the production of additional neutral pions in the showers of π^+ [17]. The response for π^+ is also greater on average than the response to p , because a large fraction of the energy of π^+ hadrons is converted to an electromagnetic shower [8, 22]. However, the \bar{p} response is significantly higher than the response to π^- , again because of the annihilation of the antiproton. FTFP_BERT does a better job of modeling this effect than QGSP_BERT because of their different descriptions of \bar{p} interactions with material.

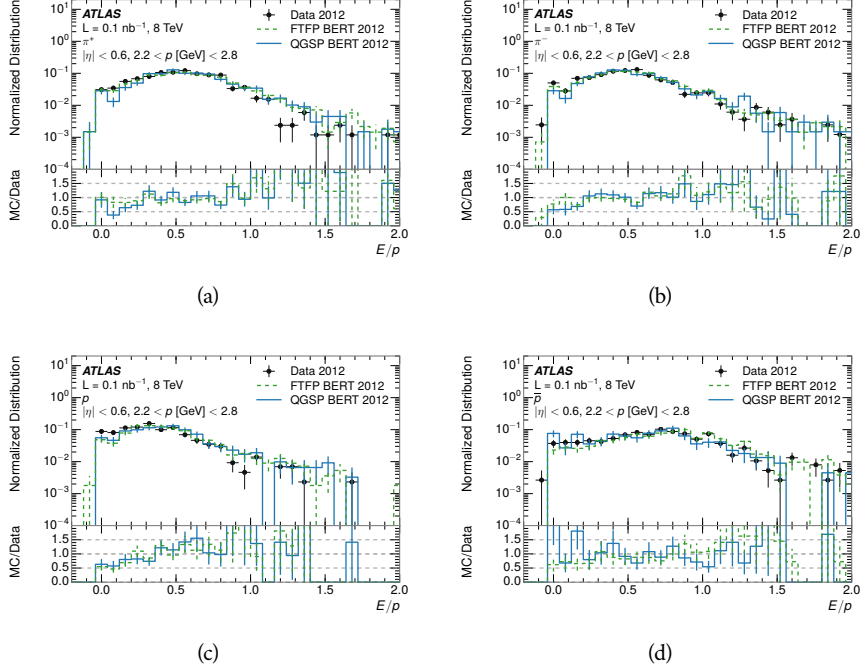


Figure 12: The E/p distribution for isolated (a) π^+ , (b) π^- , (c) proton, and (d) anti-proton tracks.

597 It is also possible to remove the neutral background from these response dis-
 598 tributions using the same technique as in Section 8.3.3. The technique is largely
 599 independent of the particle species and so can be directly applied to $\langle E/p \rangle$ for pi-
 600 ons. The $\langle E/p \rangle_{\text{COR}}$ distributions for pions are shown in Figure ??, which are very
 601 similar to the inclusive results. The inclusive hadrons are compromised mostly
 602 of pions, so this similarity is not surprising. It is also possible to see the small
 603 differences between π^+ and π^- response here, where $\langle E/p \rangle_{\text{COR}}$ is higher on av-
 604 erage for π^+ . The agreement between data and simulation is significantly worse
 605 for the π^- distributions than for the π^+ , with a discrepancy greater than 10%
 606 below 2-3 GeV.

607 8.4.3 ADDITIONAL SPECIES IN SIMULATION

608 The techniques above provide a method to measure the response separately only
 609 pions and protons. However the hadrons which forms jets include a number of
 610 additional species such as kaons and neutrons. The charged kaons are an impor-
 611 tant component of the inclusive charged hadron distribution, which is compro-
 612 mised of roughly 60-70% pions, 15-20% kaons, and 5-15% protons. These are dif-
 613 ficult to measure in data at the ATLAS detector, although a template subtraction
 614 technique has been proposed which may be effective with larger sample sizes [6].
 615 The simulation of these particles includes noticeable differences in response at
 616 low energies, which are shown in Figure 16 for FTFP_BERT. The significant dif-
 617 ferences in response between low energy protons and antiprotons are accounted
 618 for above in the definitions of E_a .

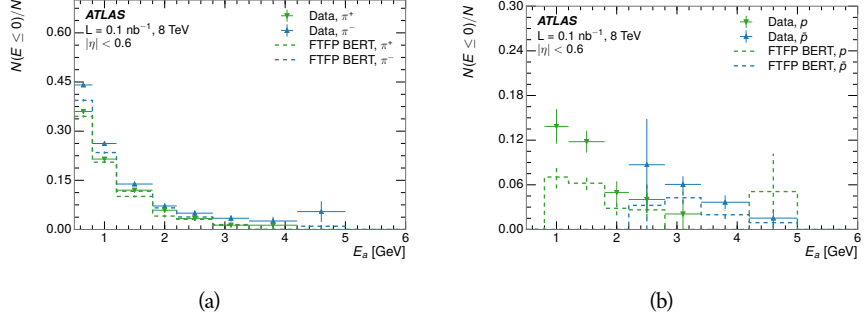


Figure 13: The fraction of tracks with $E \leq 0$ for identified (a) π^+ and π^- , and (b) proton and anti-proton tracks

619 8.5 SUMMARY

620 These various measurements of calorimeter response shown above for data and
 621 simulation illuminate the accuracy of the simulation of hadronic interactions at
 622 the ATLAS detector. The results were done using 2010 and 2012 data at 7 and 8
 623 TeV, but reflect the most current understanding of the detector alignment and ge-
 624 ometry. A number of measurements focusing on a comparison between protons
 625 and antiprotons suggest that FTFP_BERT models those interaction more accu-
 626 rately than QGSP_BERT. These measurements, among others, were the motiva-
 627 tion to switch the default Geant4 simulation from FTFP_BERT to QGSP_BERT
 628 for all ATLAS samples.

629 Even with these updates, there are a number of small, approximately 5%, dis-
 630 crepancies in response between the data and simulation at low energies. At higher
 631 energies the simulation of hadronic interactions is very consistent with data.
 632 Chapter 9 discusses how to use these observed differences to constrain the jet
 633 energy scale and its associated uncertainties.

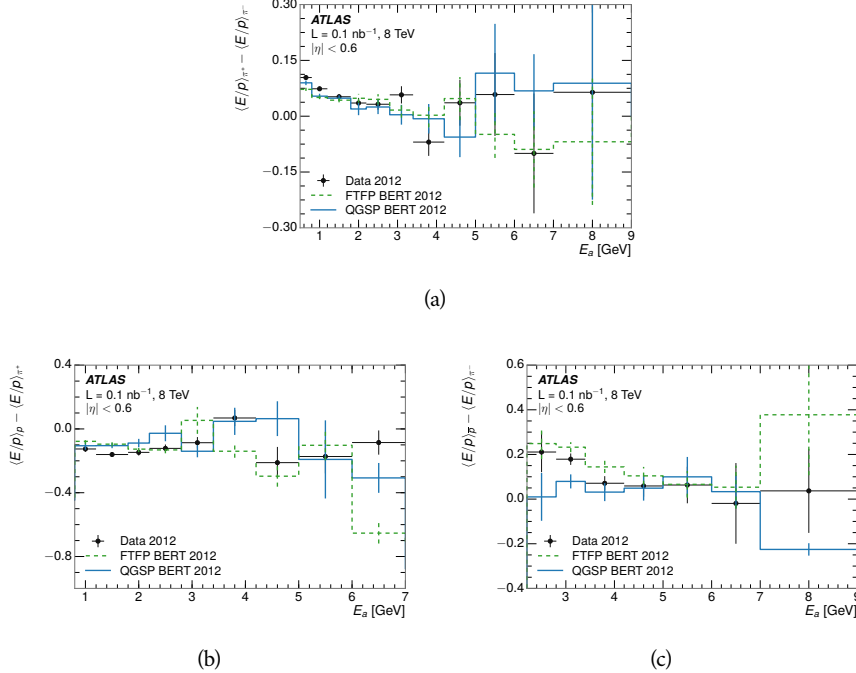


Figure 14: The difference in $\langle E/p \rangle$ between (a) π^+ and π^- (b) p and π^+ , and (c) \bar{p} and π^- .

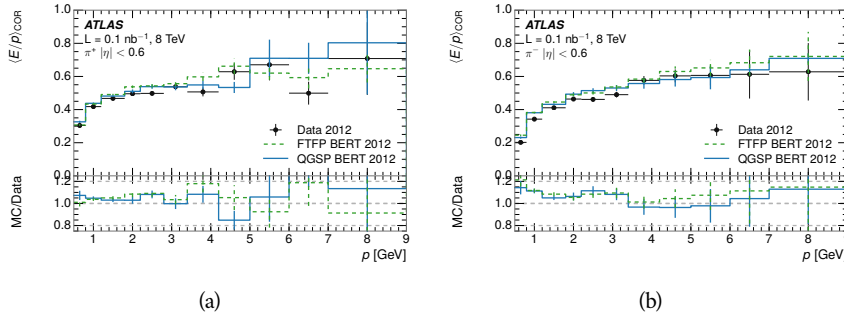


Figure 15: $\langle E/p \rangle_{\text{COR}}$ as a function of track momentum for (a) π^+ tracks and (b) π^- tracks.

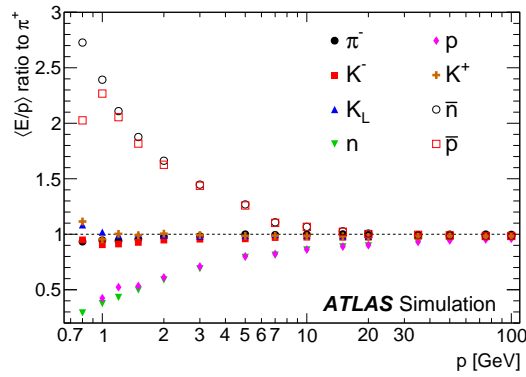


Figure 16: The ratio of the calorimeter response to single particles of various species to the calorimeter response to π^+ with the physics list FTFP_BERT.

9

634

635 JET ENERGY RESPONSE AND UNCERTAINTY

636 9.1 JET ENERGY RESPONSE IN SIMULATION

637 9.2 JET ENERGY UNCERTAINTY

638

PART V

639

SEARCH FOR LONG-LIVED PARTICLES

640

You can put some informational part preamble text here.

10

641

642 LONG-LIVED PARTICLES IN ATLAS

643 10.1 OVERVIEW AND CHARACTERISTICS

644 10.2 SIMULATION

645

646 EVENT SELECTION

647 11.1 TRIGGER

648 11.2 KINEMATICS AND ISOLATION

649 11.3 STANDARD MODEL REJECTION

650 11.4 IONIZATION

651 11.4.1 DE/DX CALIBRATION

652 11.4.2 MASS ESTIMATION

12

653

654 BACKGROUND ESTIMATION

655 12.1 BACKGROUND SOURCES

656 12.2 PREDICTION METHOD

657 12.3 VALIDATION AND UNCERTAINTY

13

658

659 SYSTEMATIC UNCERTAINTIES AND RESULTS

660 13.1 SYSTEMATIC UNCERTAINTIES

661 13.2 FINAL YIELDS

14

662

663 INTERPRETATION

664 14.1 CROSS SECTIONAL LIMITS

665 14.2 MASS LIMITS

666 14.3 CONTEXT FOR LONG-LIVED SEARCHES

667

PART VI

668

CONCLUSIONS

669

You can put some informational part preamble text here.

15

670

671 SUMMARY AND OUTLOOK

672 15.1 SUMMARY

673 15.2 OUTLOOK

674

PART VII

675

APPENDIX

676

A

677

678 INELASTIC CROSS SECTION

B

679

680 APPENDIX TEST

681 Examples: *Italics*, SMALL CAPS, ALL CAPS ¹. Acronym testing: **UML!** (**UML!**) –
682 **UML! – UML! (UML!) – UML!s**

This appendix is temporary and is here to be used to check the style of the document.

683 B.1 APPENDIX SECTION TEST

684 Random text that should take up a few lines. The purpose is to see how sections
685 and subsections flow with some actual context. Without some body copy be-
686 tween each heading it can be difficult to tell if the weight of the fonts, styles,
687 and sizes use work well together.

688 B.1.1 APPENDIX SUBECTION TEST

689 Random text that should take up a few lines. The purpose is to see how sections
690 and subsections flow with some actual context. Without some body copy be-
691 tween each heading it can be difficult to tell if the weight of the fonts, styles,
692 and sizes use work well together.

693 B.2 A TABLE AND LISTING

694 Curabitur tellus magna, porttitor a, commodo a, commodo in, tortor. Donec in-
695 terdum. Praesent scelerisque. Maecenas posuere sodales odio. Vivamus metus la-
696 cus, varius quis, imperdiet quis, rhoncus a, turpis. Etiam ligula arcu, elementum a,
697 venenatis quis, sollicitudin sed, metus. Donec nunc pede, tincidunt in, venenatis
698 vitae, faucibus vel, nibh. Pellentesque wisi. Nullam malesuada. Morbi ut tellus ut
699 pede tincidunt porta. Lorem ipsum dolor sit amet, consectetur adipiscing elit.
700 Etiam congue neque id dolor.

701 There is also a Python listing below Listing 1.

1 Footnote example.

LABITUR BONORUM PRI NO	QUE VISTA	HUMAN
fastidii ea ius	germano	demonstratea
suscipit instructior	titulo	personas
quaestio philosophia	facto	demonstrated

Table 1: Autem usu id.

702 B.3 SOME FORMULAS

Due to the statistical nature of ionisation energy loss, large fluctuations can occur in the amount of energy deposited by a particle traversing an absorber element². Continuous processes such as multiple scattering and energy loss play a relevant role in the longitudinal and lateral development of electromagnetic and hadronic showers, and in the case of sampling calorimeters the measured resolution can be significantly affected by such fluctuations in their active layers. The description of ionisation fluctuations is characterised by the significance parameter κ , which is proportional to the ratio of mean energy loss to the maximum allowed energy transfer in a single collision with an atomic electron:

*You might get unexpected results using math in chapter or section heads.
Consider the pdfspacing option.*

$$\kappa = \frac{\xi}{E_{\max}} \quad (1)$$

E_{\max} is the maximum transferable energy in a single collision with an atomic electron.

$$E_{\max} = \frac{2m_e\beta^2\gamma^2}{1 + 2\gamma m_e/m_x + (m_e/m_x)^2},$$

703 where $\gamma = E/m_x$, E is energy and m_x the mass of the incident particle, $\beta^2 =$
704 $1 - 1/\gamma^2$ and m_e is the electron mass. ξ comes from the Rutherford scattering
705 cross section and is defined as:

$$\xi = \frac{2\pi z^2 e^4 N_{Av} Z \rho \delta x}{m_e \beta^2 c^2 A} = 153.4 \frac{z^2}{\beta^2} \frac{Z}{A} \rho \delta x \text{ keV},$$

706 where

z charge of the incident particle
707 N_{Av} Avogadro's number
708 Z atomic number of the material
709 A atomic weight of the material
710 ρ density
711 δx thickness of the material
708 κ measures the contribution of the collisions with energy transfer close to
709 E_{\max} . For a given absorber, κ tends towards large values if δx is large and/or if
710 β is small. Likewise, κ tends towards zero if δx is small and/or if β approaches
711 1.

2 Examples taken from Walter Schmidt's great gallery:
<http://home.vrweb.de/~was/mathfonts.html>

Listing 1: A floating example (listings manual)

```
1 for i in xrange(10):
    print i, i*i, i*i*i
print "done"
```

712 The value of κ distinguishes two regimes which occur in the description of
713 ionisation fluctuations:

- 714 1. A large number of collisions involving the loss of all or most of the incident
715 particle energy during the traversal of an absorber.

716 As the total energy transfer is composed of a multitude of small energy
717 losses, we can apply the central limit theorem and describe the fluctua-
718 tions by a Gaussian distribution. This case is applicable to non-relativistic
719 particles and is described by the inequality $\kappa > 10$ (i. e., when the mean
720 energy loss in the absorber is greater than the maximum energy transfer
721 in a single collision).

- 722 2. Particles traversing thin counters and incident electrons under any condi-
723 tions.

724 The relevant inequalities and distributions are $0.01 < \kappa < 10$, Vavilov
725 distribution, and $\kappa < 0.01$, Landau distribution.

726 BIBLIOGRAPHY

- 727 [1] ATLAS Collaboration. “The ATLAS Simulation Infrastructure”. In: *Eur.*
728 *Phys. J. C* 70 (2010), p. 823. doi: [10.1140/epjc/s10052-010-1429-9](https://doi.org/10.1140/epjc/s10052-010-1429-9).
729 arXiv: [1005.4568 \[hep-ex\]](https://arxiv.org/abs/1005.4568). SOFT-2010-01.
- 730 [2] ATLAS Collaboration. “A study of the material in the ATLAS inner de-
731 tector using secondary hadronic interactions”. In: *JINST* 7 (2012), P01013.
732 doi: [10.1088/1748-0221/7/01/P01013](https://doi.org/10.1088/1748-0221/7/01/P01013). arXiv: [1110.6191 \[hep-ex\]](https://arxiv.org/abs/1110.6191).
733 PERF-2011-08.
- 734 [3] ATLAS Collaboration. *Summary of ATLAS Pythia 8 tunes*. ATL-PHYS-PUB-
735 2012-003. 2012. url: <http://cds.cern.ch/record/1474107>.
- 736 [4] ATLAS Collaboration. “Single hadron response measurement and calorime-
737 ter jet energy scale uncertainty with the ATLAS detector at the LHC”. In:
738 *Eur. Phys. J. C* 73 (2013), p. 2305. doi: [10.1140/epjc/s10052-013-2305-1](https://doi.org/10.1140/epjc/s10052-013-2305-1). arXiv: [1203.1302 \[hep-ex\]](https://arxiv.org/abs/1203.1302). PERF-2011-05.
- 740 [5] ATLAS Collaboration. “Electron and photon energy calibration with the
741 ATLAS detector using LHC Run 1 data”. In: *Eur. Phys. J. C* 74 (2014), p. 3071.
742 doi: [10.1140/epjc/s10052-014-3071-4](https://doi.org/10.1140/epjc/s10052-014-3071-4). arXiv: [1407.5063](https://arxiv.org/abs/1407.5063)
743 [hep-ex]. PERF-2013-05.
- 744 [6] ATLAS Collaboration. “A measurement of the calorimeter response to sin-
745 ggle hadrons and determination of the jet energy scale uncertainty using
746 LHC Run-1 pp -collision data with the ATLAS detector”. In: (2016). arXiv:
747 [1607.08842 \[hep-ex\]](https://arxiv.org/abs/1607.08842). PERF-2015-05.
- 748 [7] ATLAS Collaboration. “Topological cell clustering in the ATLAS calorime-
749 ters and its performance in LHC Run 1”. In: (2016). arXiv: [1603.02934](https://arxiv.org/abs/1603.02934)
750 [hep-ex].
- 751 [8] P. Adragna et al. “Measurement of Pion and Proton Response and Lon-
752 gitudinal Shower Profiles up to 20 Nuclear Interaction Lengths with the
753 ATLAS Tile Calorimeter”. In: *Nucl. Instrum. Meth. A* 615 (2010), pp. 158–
754 181. doi: [10.1016/j.nima.2010.01.037](https://doi.org/10.1016/j.nima.2010.01.037).
- 755 [9] S. Agostinelli et al. “GEANT4: A simulation toolkit”. In: *Nucl. Instrum. Meth.*
756 *A* 506 (2003), pp. 250–303. doi: [10.1016/S0168-9002\(03\)01368-8](https://doi.org/10.1016/S0168-9002(03)01368-8).
- 757 [10] N. S. Amelin et al. “Transverse flow and collectivity in ultrarelativistic
758 heavy-ion collisions”. In: *Phys. Rev. Lett.* 67 (1991), p. 1523. doi: [10.1103/PhysRevLett.67.1523](https://doi.org/10.1103/PhysRevLett.67.1523).
- 760 [11] N. S. Amelin et al. “Collectivity in ultrarelativistic heavy ion collisions”. In:
761 *Nucl. Phys. A* 544 (1992), p. 463. doi: [10.1016/0375-9474\(92\)90598-E](https://doi.org/10.1016/0375-9474(92)90598-E).

- 763 [12] B. Andersson, A. Tai, and B.-H. Sa. “Final state interactions in the (nuclear)
 764 FRITIOF string interaction scenario”. In: *Z. Phys. C* 70 (1996), pp. 499–
 765 506. doi: [10.1007/s002880050127](https://doi.org/10.1007/s002880050127).
- 766 [13] B. Andersson et al. “A model for low-pT hadronic reactions with general-
 767izations to hadron-nucleus and nucleus-nucleus collisions”. In: *Nucl. Phys.*
 768 *B* 281 (1987), p. 289. doi: [10.1016/0550-3213\(87\)90257-4](https://doi.org/10.1016/0550-3213(87)90257-4).
- 769 [14] H. W. Bertini and P. Guthrie. “News item results from medium-energy
 770 intranuclear-cascade calculation”. In: *Nucl. Instr. and Meth. A* 169 (1971),
 771 p. 670. doi: [10.1016/0375-9474\(71\)90710-X](https://doi.org/10.1016/0375-9474(71)90710-X).
- 772 [15] L. V. Bravin et al. “Scaling violation of transverse flow in heavy ion colli-
 773 sions at AGS energies”. In: *Phys. Lett. B* 344 (1995), p. 49. doi: [10.1016/0370-2693\(94\)01560-Y](https://doi.org/10.1016/0370-2693(94)01560-Y).
- 775 [16] L. V. Bravina et al. “Fluid dynamics and Quark Gluon string model - What
 776 we can expect for Au+Au collisions at 11.6 AGeV/c”. In: *Nucl. Phys. A* 566
 777 (1994), p. 461. doi: [10.1016/0375-9474\(94\)90669-6](https://doi.org/10.1016/0375-9474(94)90669-6).
- 778 [17] CMS Collaboration. “The CMS barrel calorimeter response to particle
 779 beams from 2 to 350 GeV/c”. In: *Eur. Phys. J. C* 60.3 (2009). doi: [10.1140/epjc/s10052-009-0959-5](https://doi.org/10.1140/epjc/s10052-009-0959-5).
- 781 [18] H. S. Fesefeldt. *GHEISHA program*. Pitha-85-02, Aachen. 1985.
- 782 [19] G. Folger and J.P. Wellisch. “String parton models in Geant4”. In: (2003).
 783 arXiv: [nucl-th/0306007](https://arxiv.org/abs/nucl-th/0306007).
- 784 [20] B. Ganhuyag and V. Uzhinsky. “Modified FRITIOF code: Negative charged
 785 particle production in high energy nucleus nucleus interactions”. In: *Czech.*
 786 *J. Phys.* 47 (1997), pp. 913–918. doi: [10.1023/A:1021296114786](https://doi.org/10.1023/A:1021296114786).
- 787 [21] M. P. Guthrie, R. G. Alsmiller, and H. W. Bertini. “Calculation of the cap-
 788 ture of negative pions in light elements and comparison with experiments
 789 pertaining to cancer radiotherapy”. In: *Nucl. Instrum. Meth.* 66 (1968), pp. 29–
 790 36. doi: [10.1016/0029-554X\(68\)90054-2](https://doi.org/10.1016/0029-554X(68)90054-2).
- 791 [22] J. Beringer et al. (Particle Data Group). “Review of Particle Physics”. In:
 792 *Chin. Phys. C* 38 (2014), p. 090001. URL: <http://pdg.lbl.gov>.
- 793 [23] V.A. Karmanov. “Light Front Wave Function of Relativistic Composite
 794 System in Explicitly Solvable Model”. In: *Nucl. Phys. B* 166 (1980), p. 378.
 795 doi: [10.1016/0550-3213\(80\)90204-7](https://doi.org/10.1016/0550-3213(80)90204-7).
- 796 [24] A.D. Martin, W.J. Stirling, R.S. Thorne, and G. Watt. “Parton distributions
 797 for the LHC”. In: *Eur. Phys. J. C* 63 (2009). Figures from the **MSTW Website**,
 798 pp. 189–285. doi: [10.1140/epjc/s10052-009-1072-5](https://doi.org/10.1140/epjc/s10052-009-1072-5). arXiv: [0901.0002](https://arxiv.org/abs/0901.0002).
- 800 [25] B. Nilsson-Almqvist and E. Stenlund. “Interactions Between Hadrons and
 801 Nuclei: The Lund Monte Carlo, Fritiof Version 1.6”. In: *Comput. Phys. Com-*
 802 *mun.* 43 (1987), p. 387. doi: [10.1016/0010-4655\(87\)90056-7](https://doi.org/10.1016/0010-4655(87)90056-7).

- 803 [26] A. Ribon et al. *Status of Geant4 hadronic physics for the simulation of LHC*
804 *experiments at the start of LHC physics program.* CERN-LCGAPP-2010-02.
805 2010. URL: <http://lcgapp.cern.ch/project/docs/noteStatusHadronic2010.pdf>.
- 806
- 807 [27] A. Sherstnev and R.S. Thorne. “Parton Distributions for LO Generators”.
808 In: *Eur. Phys. J. C* 55 (2008), pp. 553–575. doi: [10.1140/epjc/s10052-008-0610-x](https://doi.org/10.1140/epjc/s10052-008-0610-x). arXiv: [0711.2473](https://arxiv.org/abs/0711.2473).
- 809
- 810 [28] T. Sjöstrand, S. Mrenna, and P. Skands. “A Brief Introduction to PYTHIA
811 8.1”. In: *Comput. Phys. Commun.* 178 (2008), pp. 852–867. doi: [10.1016/j.cpc.2008.01.036](https://doi.org/10.1016/j.cpc.2008.01.036). arXiv: [0710.3820](https://arxiv.org/abs/0710.3820).
- 812
- 813 [29] Peter Speckmayer. “Energy Measurement of Hadrons with the CERN AT-
814 LAS Calorimeter”. Presented on 18 Jun 2008. PhD thesis. Vienna: Vienna,
815 Tech. U., 2008. URL: <http://cds.cern.ch/record/1112036>.

816 DECLARATION

817 Put your declaration here.

818 *Berkeley, CA, September 2016*

819

Bradley Axen

820

821 COLOPHON

822

Not sure that this is necessary.